SARS-CoV-2 nucleocapsid protein inhibits the stress response through RNA-binding domain N2b

Chiara Aloise, Jelle G. Schipper, Tim Donselaar, Daniel L. Hurdiss,

Raoul J. de Groot* and Frank J.M. van Kuppeveld*

Virology Division, Department of Biomolecular Health Sciences, Faculty of Veterinary Medicine, Utrecht University, 3584 CL Utrecht, the Netherlands.

* These authors share senior authorship.

Address correspondence to Raoul de Groot (R.J.deGroot@uu.nl) or Frank van Kuppeveld (F.J.M.vanKuppeveld@uu.nl)

ABSTRACT

The nucleocapsid protein N of severe acute respiratory syndrome coronavirus 2 (SARS-CoV-2) enwraps and condenses the viral genome for packaging but is also an antagonist of the innate antiviral defense. It suppresses the integrated stress response (ISR), purportedly by interacting with stress granule (SG) assembly factors G3BP1 and 2, and inhibits type I interferon responses. To elucidate its mode of action, we systematically deleted and over-expressed distinct regions and domains. We show that N via domain N2b blocks PKR-mediated ISR activation, as measured by suppression of ISR-induced translational arrest and SG formation. N2b mutations that prevent dsRNA binding abrogate these activities also when introduced in the intact N protein. Substitutions reported to block post-translation modifications of N or its interaction with G3BP1/2 did not have a detectable additive effect. In an encephalomyocarditis virus-based infection model, N2b - but not a derivative defective in RNA binding - prevented PKR activation, inhibited β-interferon expression and promoted virus replication. Apparently, SARS-CoV-2 N inhibits innate immunity by sequestering dsRNA to prevent activation of PKR and RIG-I-like receptors. Observations made for the N protein of human coronavirus 229E suggests that this may be a general trait conserved among members of other orthocoronavirus (sub)genera.

37 **SIGNIFICANCE STATEMENT**

38 SARS-CoV-2 nucleocapsid protein N is an antagonist of innate immunity but how it averts
39 virus detection by intracellular sensors remains subject to debate. We provide evidence that
40 SARS-CoV-2 N, by sequestering dsRNA through domain N2b, prevents PKR-mediated
41 activation of the integrated stress response as well as detection by RIG-I-like receptors and
42 ensuing type I interferon expression. This function, conserved in human coronavirus 229E, is
43 not affected by mutations that prevent posttranslational modifications, previously
44 implicated in immune evasion, or that target its binding to stress granule scaffold proteins.
45 Our findings further our understanding of how SARS-CoV-2 evades innate immunity, how
46 this may drive viral evolution and why increased N expression may have been a selective
47 advantage to SARS-CoV-2 variants of concern.

48 **INTRODUCTION**

49 Vertebrate cells are provided with a diversity of interconnected sensors and effectors to
50 timely detect and counter viral infection. Particularly dsRNA, an inevitable product of RNA
51 and DNA virus replication, triggers a vigorous intracellular antiviral response (1). For
52 example, binding of dsRNA by 2'-5'oligoadenylate (2-5A) synthase (OAS) leads to enzyme
53 activation and production of 2-5A, which in turn activates RNase L to stall the synthesis of
54 viral proteins through non-specific RNA degradation (2-7). Another dsRNA-activated
55 pathway, the integrated stress response (ISR) with proteinase kinase R (PKR) as key sensor,
56 entails inhibition of translation initiation and ultimately cell death. Upon dsRNA binding, PKR
57 dimerizes, autophosphorylates and then proceeds to phosphorylate the alpha subunit of
58 eukaryotic initiation factor eIF2, turning it into competitive inhibitor of guanine nucleotide
59 exchange factor eIF2b. In consequence, the production of eIF2-GTP-(Met)tRNA$_i^{Met}$ ternary
60 complex is downregulated, recognition of the initiation codon is blocked and cap-dependent
61 translation-initiation prevented (8-11). Polysome dissociation, ensuing activation of the
62 stress response, results in an excess of stalled 48S preinitiation complexes, which are stored
63 in cytoplasmic membraneless organelles called stress granules (SGs) (12-14).

64 SGs are dynamic ribonucleoprotein assemblies that are formed through liquid-liquid
65 phase separation with RNA binding protein Ras GTPase-activating protein-binding proteins 1
66 and 2 (G3BP1 and -2) functioning both as a molecular switches and main protein scaffolds
67 together with T-cell-restricted intracellular antigen 1 (TIA1) and TIA1-related protein (TIAR)
68 (15-19). The SGs thus serve as deposits from which mRNAs, poised for translation through
69 association with critical components of the translation machinery (40S ribosomal subunits,
70 eIF4E, eIF4G, eIF4A, eIF4B, Poly(A) binding protein, eIF3, and eIF2), can be rapidly retrieved.
71 SGs, however, are also considered a coordinating hub for the activation other antiviral
72 defense mechanisms like those of RIG-I-like receptors (RLRs). Indeed, RIG-I and MDA5, RLR-
73 regulating PKR-activating protein (PACT), RLR-modulating ubiquitin ligases TRIM25 and
74 TRAF2, and polyubiquitin chains are all recruited to ISR-induced SGs (20-23).

75 The antiviral mechanisms elicited by dsRNA are highly effective, even to such an extent
76 that all known mammalian viruses code for one or more antagonists (11). Coronaviruses,
77 positive-stranded RNA viruses of exceptional genetic complexity, code for a universally
78 conserved endonuclease (EndoU) that efficiently prevents simultaneous activation of host
79 cell dsRNA sensors OAS, PKR and MDA5 through dsRNA decay (24-26). Illustrating the

80 importance of EndoU, mutants defective for EndoU are attenuated in vivo, and in vitro can
81 be propagated exclusively in cells deficient in IFN-I expression or sensing, and in cells lacking
82 both RNase L and PKR (25). EndoU is derived by proteolytic processing of a large replicase
83 polyprotein pp1ab, translated from the incoming viral genome, and essential to evade early
84 innate and intrinsic antiviral host cell responses. Apparently, however, EndoU may not be
85 sufficient to suppress dsRNA-mediated antiviral activities during later stages of the viral life
86 cycle. To express the open reading frames (ORFs) downstream of the replicase gene, CoVs
87 produce a 3' co-terminal nested set of subgenomic mRNAs from which the structural
88 proteins are translated in addition to a variety of so-called accessory non-structural
89 proteins. Some of the latter also have been shown to counteract dsRNA-mediated antiviral
90 host responses. For example, the ns4a protein of Middle East Respiratory Syndrome
91 coronavirus (MERS-CoV) prevents PKR-mediated stress by sequestering dsRNA (27, 28),
92 whereas the MERS-CoV ns4b protein is a phosphodiesterase (PDE) and antagonizes the OAS-
93 RNase L pathway by enzymatically degrading 2-5A activators (29). Non-related PDEs, ns2
94 proteins, are found in members of the subgenus *Embecovirus*, including human coronavirus
95 OC43 (30). Finally, a specific inhibitor of the ISR was found in gammacoronaviruses of
96 cetaceans. The beluga whale coronavirus accessory protein 10 (BWCoV acP10) blocks p-eIF2-
97 eIF2B association to allow continued formation of the ternary complex and unabated global
98 translation even at high p-eIF2 levels that would otherwise cause translational arrest (31).
99 Apparently, CoVs rely on redundancy in antagonists and antagonistic mechanisms to
100 effectively counter dsRNA-induced antiviral host responses. Likewise, the current pandemic
101 severe acute respiratory syndrome coronavirus 2 (SARS-CoV-2) codes for an ISR inhibitor
102 additional to EndoU (32). Its nucleocapsid protein (N) was reported to block the ISR and to
103 inhibit SG formation in a PKR- and G3BP1-dependent fashion (33-35). In apparent
104 concordance, proteomics studies and structural analyses provided evidence for physical
105 interactions between N and the SG key components G3BP1 and G3BP2 (33, 36-39).
106 Coronavirus N proteins have a modular structure with N-terminal and C-terminal RNA-
107 binding domains, called N1b and N2b respectively, bounded by largely disordered regions.
108 Here, we took a reductionistic approach involving systematic deletion and individual
109 transient expression of the different regions and domains. We show that the N2b domain is
110 critical and sufficient to counter the ISR. Single site mutations in N2b that block dsRNA
111 binding prevent PKR activation. This activity is not affected by posttranslational

modifications elsewhere in the N protein that are known to regulate RNA binding nor dependent on physical interaction with G3BP1 and G2BP2. Using the encephalomyocarditis virus as a surrogate infection system we show that N2b domain prevents PKR-mediated activation of the ISR and suppresses IFNβ expression also in virus-infected cells. Our findings suggest that in addition to a function in replication and genome packaging, SARS-CoV-2 N functions as a classical antagonist of dsRNA-induced host defense.

119 **RESULTS**

120

121 **SARS-CoV-2 N inhibits PKR-induced ISR.** Previously, we showed that transfection of cells
122 with specific expression plasmids like pEGFP-N3 may trigger the ISR through dsRNA-
123 mediated PKR activation, resulting in translation arrest and the formation of SGs. This
124 phenomenon allows for a convenient method to identify potential viral ISR antagonists by
125 transiently expressing these proteins genetically fused to enhanced green fluorescent
126 protein (EGFP) (27). The expression levels of these fusion proteins can then be compared to
127 that of EGFP alone while SG formation can be assessed by immune fluorescence analysis
128 (IFA) by staining the transfected cells for established SG markers like G3BP2 or eIF3. While
129 using this procedure to probe SARS-CoV-2 proteins for a potential role in ISR inhibition, we
130 noted suppression of SG formation in cells expressing nucleocapsid protein N. Like the well-
131 established PKR antagonists influenza A virus (IAV) ns1 and MERS-CoV ns4a, SARS-CoV-2 N
132 significantly reduced the number of transfected cells with stress granules both in HeLa as
133 well as in A549 cultures (Fig. 1A). Moreover, expression levels of the SARS-CoV-2 N-EGFP
134 fusion protein were strongly increased as compared to the EGFP control, indicative for
135 suppression of ISR-induced translational arrest. Again, like IAV ns1 and MERS-CoV ns4a, but
136 unlike AcP10 of beluga whale CoV, N-GFP had only a modest effect on SG formation in
137 arsenite-treated cells (Fig. 1B). The results are consistent with SARS-CoV-2 N inhibiting the
138 ISR and SG formation by acting as a PKR inhibitor.
139 The N protein of another betacoronavirus, MERS-CoV, was previously noted to suppress
140 SG formation too (35). Interestingly, we observed inhibition of translational arrest and SG
141 formation also in cells expressing the N protein of human alphacoronavirus 229E (HCoV-
142 229E) (Fig. 1 C). Apparently, N-mediated suppression of the ISR is not unique to
143 betacoronaviruses but may well be a general trait conserved among members of other
144 orthocoronavirus (sub)genera.

145

146 **Domain N2b is essential and sufficient for suppression of SG formation.** The N proteins
147 from the four CoV genera share only 27 to 30% sequence identity but are conserved in their
148 modular organization (Fig.2A) ((40, 41) for a review see (42)). They are comprised of two
149 ordered domains, the N-terminal domain (N1b also called NTD) and the C-terminal domain
150 (N2b aka CTD) (in SARS-CoV-2 N, residues 49-175 and 247-365, respectively). N1b and N2b

151 are separated and flanked by segments, predicted to be at least partially disordered (N1a,
152 N2a and N3). N1b and N2b have been implicated in RNA binding and, in case of N2b, also in
153 N dimerization. Indeed, in infected cells and upon heterologous expression, CoV N proteins
154 form homodimers that, in turn, assemble into tetramers mediated by N3 (43). The N2a
155 central spacer contains a serine- and arginine-rich (SR) region, immediately downstream of
156 N1b, the regulated phosphorylation of which is deemed important for N function during
157 different stages of the CoV replication cycle (44-46). The primary function of N is in virus
158 assembly. It condenses newly produced gRNA into helical nucleocapsids, apparently with
159 N2b controlling target selectivity (47, 48), and then drives envelopment by binding to the
160 viral membrane protein M via N3. However, N has several functions auxiliary to virion
161 morphogenesis. At the very start of the infectious cycle, N is essential for the initiation of
162 infection by the incoming gRNA through association of SR with the cytosol-exposed
163 ubiquitin1 domain of replication organelle pore protein nsP3 (46, 49). Moreover,
164 purportedly relevant to ISR suppression, N binds to G3BP1 and 2 through segment N1a (39,
165 50, 51).
166 To determine the molecular basis for ISR suppression, we constructed a library of N
167 mutants with partially disordered regions and domains either systematically deleted or
168 expressed in isolation. As shown in **Fig. 2**, suppression was lost upon deletion of subdomain
169 N2b. Moreover, expression of N2b in isolation caused a reduction in SGs to an extent similar
170 to that of full-length N. The data therefore suggested that ISR inhibition and SG suppression
171 as observed for the intact N protein is mediated at least in part by N2b.
172
173 **N2b mutations that disrupt dsRNA binding abrogate suppression of SG formation.** N2b
174 binds both single and double stranded oligonucleotides, whether RNA or DNA (42, 52, 53).
175 Hence, a possible mechanism for N2b to prevent PKR-induced activation of the ISR is by
176 sequestering dsRNA. Crystal structural analysis revealed that N2b homodimers form a
177 rectangular slab with wide faces of 45 Å × 35 Å in dimension (52). One is comprised of an
178 interlaced inter-molecular four-stranded β-sheet and predominantly negatively charged, the
179 other of two α-helical regions separated by a shallow central, positively charged groove
180 thought to be the oligonucleotide binding site (42, 52, 54, 55). Within the groove, there are
181 several conserved positively charged residues with their surface-exposed side chains
182 seemingly poised for interaction with nucleic acid, in particularly Lys^{257} and Lys^{261} (**Fig. 3A**).

183 The binding by bacterially-expressed N2b of synthetic RNA oligonucleotides, whether single
184 or double-stranded, SARS-CoV-2 derived (highly conserved 3' UTR stem-loop II motif, s2m;
185 (56)) or a scrambled version thereof, can be readily demonstrated by electrophoretic
186 mobility assay (EMSA) (Fig. 3B).
187 To test whether Lys^{257} and Lys^{261} are involved in RNA binding and whether such binding is
188 important to counteract the ISR and suppress SG formation, they were replaced by Ala,
189 separately and in combination. Indeed, dsRNA binding was either significantly reduced or
190 lost beyond detection upon substitution of Lys^{257} and Lys^{261}, respectively (Fig. 3B). In
191 accordance, Ala substitution of Lys^{261} and Lys^{257} failed to rescue protein synthesis (Fig. 3C)
192 and reduced SG suppression either in almost all or in about 60% of the transfected HeLa
193 cells, respectively (Fig. 3D). Notably, Ala substitution of other surface-exposed charged
194 residues (Gln^{272}, Gln^{289}, Arg^{276}, Arg^{293}), not located within the RNA binding groove but rather
195 implicated in N2b inter-dimer association (42, 53), did not detectably affect SG formation
196 (Fig. 3D).
197 Importantly, also in the intact N protein, Lys^{261}Ala substitution abrogated inhibition of
198 translational arrest as well as SG formation and so did the Lys^{257}Ala mutation (Fig. 3C, D). It is
199 unknown why the latter mutation exerts a stronger effect in the context of the full-length
200 protein than in N2b. The combined data, however, do show that Lys^{261} and Lys^{257} are
201 required for nucleic acid binding by N2b and suggest that this capacity to bind RNA is
202 essential for SG suppression. Moreover, the observation that also for the intact N protein SG
203 suppression was reduced to background levels by single site Lys^{261}Ala and Lys^{257}Ala
204 substitutions suggests that ISR inhibition by SARS-CoV-2 N critically relies on N2b and N2b-
205 mediated RNA binding. Notably, the N protein of alphacoronavirus HCoV-229E also lost its
206 capacity to block SG formation when the orthologous N2b residues, Lys^{246} and Lys^{250}, were
207 substituted (Fig. 3D), suggestive of a common mechanism for ISR inhibition through the
208 binding of RNA.
209
210 **N2b-mediated inhibition of SG formation is not affected by posttranslational modifications**
211 **of N nor by disruption of the G3BP1/2 binding motif.** Previous studies identified N as a
212 multifunctional protein involved in different aspects of the viral replication cycle beyond
213 viral assembly. Its activity apparently is regulated by posttranscriptional modifications such
214 as differential phosphorylation of the SR domain, which alters RNA binding affinity (57, 58),

215 and acetylation at Lys^{375}, reportedly essential for liquid–liquid phase separation of N-RNA
216 ribonucleoprotein complexes (59). Arginine methylation of SARS-Cov-2 nucleocapsid protein
217 at Arg^{95} and Arg^{177} was reported to regulate RNA binding and its ability to suppress stress
218 granule formation (33). Moreover, an ΦxFG motif within N1a (residues 15-18), required for
219 association with G3BP1 and 2 (39), was recently proposed to rewire the G3BP1/2
220 interactome to disrupt stress granules (37).
221 To test the importance of each of these posttranscriptional modifications as well as of
222 G3BP1/2 interaction on N2b-mediated inhibition of SG formation, we performed site-
223 directed mutagenesis. Suppression of SG formation by the full-length N protein was not
224 affected by Ala substitution of Arg^{95}, of $Arg^{276}$and Arg^{293} combined, or of Lys^{375} nor by
225 disruption of the N1a ΦxFG motif (51) through joined substitution of Arg^{14} and Ile^{15} (**Fig. 4**).
226 An N derivative in which phosphorylation of the SR segment was prevented through Ala
227 substitution of 13 out of 14 Ser residues (13S>A) displayed a cellular distribution distinctively
228 different from that of the parental wildtype protein, accumulating in large aggregates
229 together with G3BP1 and often also eIF3. These deposits differed in size and appearance
230 from typical SG, complicating the interpretation of the data. Importantly, however, the
231 expression levels of the N-13S>A mutant were like those of wildtype N, as judged by
232 fluorescence intensity observed in IFA, and consistently higher than those of EGFP (data not
233 shown). We interpret the findings to indicate that the SR mutations may cause the N protein
234 to aggregate but not to affect inhibition of ISR-induced translational arrest.
235
236 **Suppression of PKR-induced ISR by coronavirus N proteins is mediated predominantly by**
237 **N2b.** To corroborate our observations, we measured N-mediated rescue of ISR-induced
238 translational arrest also by flow cytometry. To this end, we used a cotransfection assay with
239 red fluorescence protein (RFP) expressed from vector pcDNA-RFP serving as reporter
240 (Rabouw et al., 2016). Co-transfection with ISR-inducing plasmid pEGFP-N3 strongly inhibited
241 RFP production (**Fig. 5**, top; see also **Fig. S1**). RFP expression was rescued in cells co-
242 expressing N2b but not by its RNA-binding deficient derivative N2b-K^{257}A/K^{261}A. RFP
243 expression was also rescued by the intact N proteins of either SARS-CoV-2 or HCoV-229E and
244 to similar levels by SARS-CoV-2 N mutants defective for G3BP1/2 binding (N-R^{14}A/I^{15}A) or
245 N1b methylation (N-R^{95}K) (**Fig. 5**). In contrast, inactivation of N2b through the K^{257}A/K^{261}A
246 double mutation in the intact N protein of either SARS-CoV-2 or HCoV-229E significantly

247 reduced RFP expression (Fig. 5). Intriguingly, however, RFP expression levels were still higher
248 than those observed for EGFP (p-value 0.0014) or N2b-$K^{257}A/K^{261}A$ (p-value 0.0195). The data
249 suggest that suppression of the ISR by coronavirus N proteins is mediated predominantly by
250 the N2b domain though not exclusively. Apparently, N counteracts translational arrest also
251 through other domains via alternative mechanisms, but this contribution only becomes
252 detectable upon N2b inactivation. Remarkably, substitutions in segment N1a known to
253 disrupt N-G3BP1/2 interactions (51) did not have an additive effect when tested in
254 combination with the N2b mutations (Fig. 5; panel 'SARS2 N N1a-N2b mut').

255

256 **N2b-mediated suppression of the ISR and type I interferon response in virus-infected cells.**
257 Whereas the results provide conclusive evidence for ISR suppression upon transient
258 expression of N in transfected cells, the question arises whether this phenomenon also
259 occurs during natural infection and whether it is relevant for evasion of the innate host
260 immune response. Unfortunately, the essential functions of N at multiple stages of the
261 coronavirus life cycle, both during early replication as well was in genome packaging during
262 virion assembly, precludes a straightforward reverse genetics approach. Thus, the
263 construction of recombinant SARS-CoV-2 mutants with an N protein defective in N2b RNA
264 binding was deemed a nonviable option. We therefore resorted to a well-established
265 alternative model based on recombinant encephalomyocarditis virus mutant EMCV-L^{zn}, in
266 which the autologous ISR antagonist (the leader protein L) is inactivated. The mutant virus is
267 no longer able to counteract the ISR and hence provides a convenient platform to identify
268 and characterize ISR antagonists of other viruses.
269 Our initial experiments were performed with an EMCV mutant that coded for a chimeric
270 polyprotein with N2b at its N-terminus, genetically fused to residues 1 through 5 of EMCV L^{zn}
271 plus two additional residues encoded by an engineered *Xho*I site . This virus, however, failed
272 to suppress the ISR. We noted that in the fusion protein, two negatively charged residues, E^6
273 (from L) and E^8 (encoded by the *Xho*I sequence) are immediately upstream of N-terminal
274 N2b residues K^{248} and K^{249} (residues 9 and 10 of the chimera) and proximal to critical N2b
275 residues K^{257} and K^{261} Fig. S2). Arguing that this might affect N2b RNA binding, we introduced
276 into the EMCV-L^{zn} genome an N-terminally extended N2b with the N2a region serving as a
277 spacer (Fig. 6A, Fig. S2). Indeed, in cells, infected with the resulting virus EMCV-L^{zn}-

278 N2aN2b^{wt}, SG suppression was restored to 70% of that of wildtype EMCV, i.e. to levels
279 similar to those reported for EMCV derivatives with L replaced by established PKR inhibitor
280 MERS-CoV ns4a (**Fig. 6B, C**). In accordance, in cells infected with the N2aN2b^{wt} virus , levels
281 of phosphorylated PKR were consistently low, comparable to those in mock- or in wildtype
282 EMCV-infected cells and 3 to 4 fold lower than those in cells infected with EMCV-L^{zn-}. Thus, in
283 its activity N2aN2b^{wt} mimicked MERS-CoV ns4a which prevents PKR activation by
284 sequestering dsRNA (27) but differed from AcP10 which inhibits the ISR at a level
285 downstream of PKR (31). Like MERS-CoV ns4a and AcP10, N2aN2b restored replication
286 efficacy of EMCV-L^{zn} to near wildtype levels as based on expression of the viral capsid
287 proteins (**Fig. 6D**). To test whether N2aN2b, like ns4a, also suppresses the type I interferon
288 response, levels of IFN-β mRNA were determined by qRT-PCR. Indeed, in cells infected with
289 EMCV-L^{zn}-N2aN2b^{wt} IFN-β expression was reduced as compared to EMCV-L^{zn} infected cells to
290 levels observed in cells infected with EMCV wt or EMCV-L^{zn}-MERS-ns4a (**Fig. 6E**). In contrast,
291 in cells infected with EMCV-L^{zn}-N2aN2b-K^{257}A+K^{261}A, encoding an inactive N2b, there was no
292 detectable suppression of SG formation, PKR was phosphorylated, and viral replication was
293 delayed to similar if not larger extent than in EMCV-L^{zn}-infected cells (**Fig. 6B-D**). EMCV-L^{zn}-
294 N2aN2b-K^{257}A+K^{261}A also lost the capacity to suppress the type I IFN response although this
295 was noticeable only at 8 hr post infection (**Fig. 6E**), which may be attributed to the
296 considerable delay in virus replication and a consequential late onset of IFN induction.
297 We conclude that SARS-CoV-2 N2b functions as an antagonist of the ISR in EMCV-infected
298 cells and can functionally replace the EMCV L protein by acting as a classical PKR antagonist
299 and preventing activation of the ISR by sequestering dsRNA. This mode of action differs from
300 that of beluga whale CoV AcP10 and Aichivirus L, which counteract the ISR by salvaging
301 global translation through competitive inhibition of p-eIF2–eIF2B association (31). The data
302 lend support to the notion that N through N2b may inhibit the ISR and SG formation also in
303 the context of SARS-CoV-2-infected cells.

304 **DISCUSSION**

305 To successfully establish infection, viruses must subdue the intracellular host defense
306 long enough to complete their replication cycle and vigorously enough to prevent the
307 infected cells from raising the alarm. The detection of dsRNA, an inevitable byproduct of
308 both RNA and DNA virus replication is central to activation of the innate antiviral defense.
309 The activation of RLRs must be averted that would otherwise culminate, through intra- and
310 intercellular signaling, in the production of type I interferons and other proinflammatory
311 cytokines. Also, while host cell protein synthesis should best be inhibited and kept at a
312 minimum, efficient unperturbed production of viral proteins must be ensured by preventing
313 translational suppression due to activation of the OAS/RNaseL pathway and PKR-dependent
314 induction of the ISR. Recent publications implicated SARS-CoV-2 N protein as an inhibitor of
315 SG formation and an RLR antagonist (33-35, 60-62). Here, we confirmed and extended these
316 observations using a convenient procedure to assess PKR-induced ISR activation based on
317 transfection of ISR-inducing plasmid DNA to drive the expression of putative ISR antagonists
318 genetically fused to EGFP. We showed by IFA that SARS-CoV-2 N inhibits translational arrest
319 and ensuing SG formation and corroborated our findings by flow cytometry. Moreover, we
320 showed that the N protein of human alphacoronavirus 229E (subgenus *Duvinacovirus*) also
321 prevents translational arrest and suppresses SG formation to similar extent and via a similar
322 mode of action. These findings suggest that this property may yet be widely conserved
323 among members of different orthocoronavirus (sub)genera.

324 To study the mechanism of ISR inhibition, we performed a systematic deletion and site-
325 directed mutational analysis of SARS-CoV-N. We found that inhibition of SG formation was
326 lost upon deletion of N2b in accordance with findings of Zheng et *al.*, (35). However, we
327 crucially extend their observations by showing that N2b when expressed in isolation, is
328 sufficient to impair transfection-induced ISR-mediated translational shut off as well as the
329 formation of SGs. Apparently, N2b counteracts the ISR by binding dsRNA. Ala substitution of
330 conserved Lys residues (Lys^{257} and/or Lys^{261}) in the RNA-binding cleft of N2b that abolished
331 dsRNA binding also abolished ISR inhibition. Importantly, these substitutions also caused the
332 intact N proteins of SARS-CoV-2 and HCoV-229E to lose their activity as ISR antagonists. The
333 observations thus strongly support a model in which coronavirus N proteins through their
334 N2b domain prevent activation of the ISR by PKR by sequestering dsRNA, like the other viral
335 PKR inhibitors IAV ns1 and MERS-CoV ns4a that were used as controls throughout.

336 The N protein plays a crucial role during the very early steps of the CoV infection cycle
337 (52, 63-65) and is indispensable for virus morphogenesis. Evidently, this impedes a direct
338 mutational reverse genetics approach to study the occurrence and relevance of N-mediated
339 inhibition of the ISR in CoV-infected cells. However, by using a mutant EMCV as a platform,
340 we showed that an extended protein N2aN2b can functionally replace the autologous
341 enterovirus L protein and can salvage the EMCV replication defect caused by L inactivation,
342 like we previously showed for MERS-CoV ns4a and BWCoV ACP10 (27, 31). Like MERS-CoV
343 ns4a, but unlike BWCoV AcP10 -which blocks the ISR downstream of PKR-, N2aN2b
344 prevented PKR phosphorylation apparently via N2b-mediated RNA binding. The findings
345 provide proof of principle that N2b can promote viral replication by preventing PKR and
346 ensuing ISR activation, supporting the notion that N through its N2b domain may do so as
347 well during CoV infection.
348 Adding relevance to our observations, selection for enhanced innate immune escape
349 apparently favored SARS-CoV-2 variants with increased N expression (66). Moreover, a
350 three-nucleotide change in Gamma also present in Alpha and Omicron variants of concern
351 created a new (cryptic) transcription regulating sequence to drive the synthesis of a novel
352 subgenomic mRNA species from which a truncated N-protein, N*, may be translated
353 corresponding with the C-terminus of the protein and initiating at in frame Met^{210} (66, 67). If
354 N* is indeed expressed, our findings strongly support a role in dsRNA sequestration and
355 innate antagonism.
356 The native coronavirus N proteins are subject to extensive posttranslational modifications
357 in domains and segments other than N2b. Some have been implicated in liquid-liquid phase
358 separation (59, 68), RNA binding (33), SG formation and inhibition of innate immunity (33,
359 59), prompting the question whether these modifications promote or hinder its function as
360 an ISR antagonist. Reportedly, methylation of Arg^{95} in the SARS-CoV-2 N1b segment by host
361 protein arginine methyltransferases is required for RNA binding and for the inhibition of
362 arsenite-induced formation of G3BP1-containing SGs (33). In our hands, however, an N
363 mutant with Arg^{95}Lys substitution, described to block N-mediated suppression of SGs (33),
364 still prevented PKR-induced ISR-associated translational repression to identical extent as the
365 wildtype protein and likewise prevented SG formation. In another recent study, Wang et *al.*
366 (59) reported suppression of MAVS signaling by intact SARS-CoV-2 N protein but not by an N
367 derivative from which N2b had been deleted. They attributed this to N-induced and N2b-

368 dependent liquid-liquid phase separation (LLPS) subject to acetylation of N3 residue Lys^{375}.
369 In accordance, we find that in EMCV-infected cells, N2aN2b, like MERS4a, suppresses β-
370 interferon (IFN-β) expression and show that this activity is blocked by mutations that abolish
371 N2b-mediated RNA binding. In apparent contrast to the observations of Wang et *al*. (59),
372 however, we find that acetylation of Lys^{375} is not essential for RNA binding by N2b and that
373 Lys^{375}Arg substitution does not detectably affect inhibition of the PKR-induced ISR by the
374 intact N protein. Our findings suggest that N through autonomous activity of the N2b
375 domain acts not only as a classical PKR inhibitor to thwart ISR activation but -by shielding
376 dsRNA- may also prevent RLR activation and thus block induction of the type I IFN response.
377 Our conclusions would seem at odds with the firmly established physical interaction with
378 N and SG scaffold proteins G3PB1 and -2 (33, 38, 39, 51, 69) which would suggest a role of
379 this interaction in SG suppression. The findings may be reconciled, however, by assuming
380 that coronavirus N proteins have been evolutionary selected to interfere with the formation
381 and function of SGs through distinct mechanisms at multiple levels during different stages of
382 the viral life cycle, mediated by different domains and regulated by distinct posttranslational
383 modifications. Possibly, such subtleties are missed in over-expression experiments and
384 overshadowed by the robust ISR inhibition by N2b. G3BP1/2-N association through
385 subdomain N1a (39, 50, 51) and N2b, directly via protein-protein interaction and/or
386 indirectly, promoted by RNA binding (70), may well hamper SG assembly and/or thereby
387 impede recruitment and SG-facilitated activation of RLRs and PKR (20-23) already early in
388 infection when levels of N are still low. Indeed, this would be consistent with observations by
389 others (35, 70) that SARS-CoV-2 inhibits induction of type I IFNs by targeting G3BP1 and
390 suppressing SG-associated RLR activation. It has also been proposed that N counteracts the
391 intracellular antiviral response by interfering with innate immune signaling at the level of
392 MAVS and impeding MAVS-RIG-I association (59). The relative importance of these and
393 other activities of N for suppression of innate immunity during coronavirus infection clearly
394 requires further study as well as the interplay with other viral antagonists of innate
395 responses such as EndoU (25), SARS-CoV-2 ns6 (71, 72) and ns9b (66, 67).
396

397 **MATERIALS AND METHODS**

398

399 **Cell lines.** HeLa-R19, A549 and BHK21 cells were maintained in Dulbecco's Modified Eagle's
400 Medium (DMEM) supplemented with 10% (V/V) fetal calf serum (FCS) and 100 units/ml
401 penicillin and streptomycin.

402 **Recombinant EMCV viruses.** Recombinant EMCV viruses were derived from the pM16.1-
403 derived pStrep2-VFETQG-Zn-M16.1 infectious clone (27, 73). This vector carries a Zn-finger
404 mutation to inactivate EMCV L as well as coding sequences for a Strep2-tag and a synthetic
405 optimized 3Cpro recognition site (VFETQG). The coding sequences for N2b and N2a2b were
406 PCR amplified from SARS-CoV-2-derived cDNA (sequences deposited in EVA database; Ref-
407 SKU: 026V-03883) and inserted into XhoI/NotI-digested pStrep2-VFETQG-Zn-M16.1 yielding
408 pStrep2-SARS-CoV-2-N2b-VFETQG-Zn-M16.1 and pStrep2-SARS-CoV-2-N2aN2b-VFETQG-Zn-
409 M16.1, respectively. Mutations to substitute N2b Lys^{257} and Lys^{261} by Ala were introduced by
410 Q5 side-directed mutagenesis (New England Biolabs, NEB) generating pStrep2-SARS-CoV-2-
411 N2aN2b $K^{257}A/K^{261}A$-VFETQG-Zn-M16.1. The vectors were linearized with BamHI, used for *in*
412 *vitro* transcription with the RiboMAX kit (Promega) and the resulting RNA was purified using
413 the NucleoSpin RNA mini kit (Machery-Nagel) following the manufacturer's protocol. Viruses
414 were recovered by transfecting BHK-21 cells, grown to subconfluency in T125 flasks, with 1.5
415 µg of the run-off RNA transcripts using Lipofectamine2000 (Invitrogen) transfection reagent
416 according to the manufacturer's protocol. After 2-4 days, when total cytopathic effect was
417 apparent, the cultures were subjected to three freeze-thaw cycles, cell debris was pelleted
418 at 4,000x*g* for 15 minutes and virus was concentrated from the supernatants by
419 ultracentrifugation though a 30% sucrose cushion at 140,000x*g* for 16 hours at 4°C in a
420 SW32Ti rotor. Virus pellets were resuspended in phosphate-buffer saline (PBS). The viruses
421 were characterized by isolating viral RNA from 150-µL aliquots of the cell culture
422 supernatant with the NucleoSpin RNA Virus kit (Macherey-Nagel) followed by conventional
423 RT-PCR and bidirectional Sanger sequence analysis of the inserted SARS-CoV-2 sequences
424 and flanking regions. Viral titers, determined by endpoint titration and calculated by the
425 Spearman-Kaerber formula, are averages from three independent experiments.

426 **Plasmids for eukaryotic and prokaryotic expression.** Eukaryotic expression plasmids were
427 constructed by cloning PCR-amplified sequences of interests, flanked by NheI and BamHI
428 restriction sites, into NheI/BamHI digested vector pEGFP-N3 (ClonTech) such that the
429 encoded viral proteins are C-terminally fused to enhanced green fluorescent protein (EGFP).
430 pcDNA-RFP was purchased from Addgene.
431 Procaryotic expression plasmid pGEX2T-Hisx6-N2b encoding N-terminally His-tagged
432 SARS-CoV-2 N2b was created by linearizing vector pGEX2T, amplifying the N2b coding
433 sequences by Q5-PCR, and assembling the fragments by NEBuilder HiFi DNA Assembly (NEB)
434 according to the manufacturer's instructions. Mutations (N2b $K^{257}A$, N2b $K^{261}A$ and N2b
435 $K^{257}A+K^{261}A$) were generated by Q5 site-directed mutagenesis (New England Biolabs, NEB).
436 All constructs were sequenced to confirm their integrity.
437
438 **Immunofluorescence assay.** HeLa-R19 and A549 cells were seeded onto 12 mm glass cover
439 slips in 24-well plates (Corning Costar) at $5x10^4$ cells and grown for 24 hr. They were then
440 transfected with 500 ng total DNA/well using Lipofectamine2000 (Invitrogen) according to
441 the instructions of the manufacturer. At 24 hr post transfection, cells were either left
442 untreated or treated with 500 µM sodium arsenite ($NaAsO_2$, Riedel-de Haën) for 30 min at
443 37°C and subsequently fixed in PBS + 3.7% paraformaldehyde (PFA). HeLa-R19 cells were
444 infected with recombinant EMCV viruses at a multiplicity of infection (MOI) of 10 $TCID_{50}$/cell
445 and incubated for 6 or 8 hr. Cells were fixed with paraformaldehyde (3.7% in PBS), incubated
446 with PBS + 0.1% glycine for 10 min to quench the fixative, permeabilized with 0.1% Triton X-
447 100/PBS+s for 10 min at RT and subsequently blocked in blocking buffer (PBS + 1% BSA +
448 0.1% Tween-20) for 30min in a dark humidified chamber at 37°C. The cells were then
449 incubated in blocking buffer containing mouse anti-dsRNA (1:1000; English & Scientific
450 Consulting), goat anti-eIF3η (1:200, SantaCruz) and rabbit anti-G3BP2 (1:200; Bethyl
451 Laboratories) for 1h at room temperature (RT). After three washing steps with
452 PBS+0.1%Tween-20, cells were incubated with secondary antibody donkey anti-mouse Cy2
453 (1:100; The Jackson Laboratory), donkey anti-goat Alexa594 (1:200; Invitrogen), donkey anti-
454 rabbit Alexa647 (1:200; Invitrogen) in block buffer for 1h at RT. The cells were then washed
455 three times with PBS+0.1%Tween-20, once with distilled water and mounted on glass
456 microscope slides in ProLong Diamond Antifade (Invitrogen) mounting medium. Cells were
457 examined by conventional wide-field (Olympus) and confocal immunofluorescence

458 microscopy (Nikon A1R) in most cases also in a blinded fashion by a second independent
459 observer.
460
461 **Flowcytometry analysis.** HeLa cells were seeded in a 12-well cluster (10^5 cells/well) and,
462 after overnight incubation, transfected with the indicated plasmids (500 ng well; 250
463 ng/plasmid) using Lipofecatmine2000 (Invitrogen) according to the manufacturer's
464 instructions. At 24 hr post transfection, cells were detached with trypsin, washed once PBS,
465 and fixed in PBS, 3.7% PFA for 10 min. The samples were washed once in FACS buffer (PBS +
466 0.02% Na-azide and 0.5% BSA) and kept in FACS buffer at 4ºC. RFP fluorescence intensity was
467 recorded with a CytoFLEX LX flow cytometer (Beckman Coulter) and the data were analyzed
468 by FlowJo™ v10 software (BD Biosciences). Samples were gated for live single cell
469 populations and then gated for negative, low (L) and high (H) RFP expressing cells. For bar
470 graphs [H/L] ratios were normalized with the ratio calculated for the relevant wildtype
471 protein set at 100%.
472
473 **Electrophoretic Mobility Shift Assay (EMSA).** To purify the wildtype N2b domain and its
474 mutated derivatives, *E. coli* BL21 cells (Sigma-Aldrich), transformed with pGEX2T-Hisx6-N2b
475 or its mutated derivatives, were grown in LB medium containing ampicillin (50 µg/ml) at
476 37°C until the optical density at 600 nm (OD_{600nm}) reached 0.3. The temperature was then
477 reduced to 18°C, and when the OD_{600nm} reached 0.5, protein expression was induced with
478 0.5 mM IPTG. Following expression for 16 hours, the cells were harvested by centrifugation
479 and resuspended in lysis buffer (100 mM Tris-HCl pH=8, 300 mM NaCl, 10 mM imidazole,
480 0.1% Triton X-100, 5% Glycerol) complemented with lysozyme (0.25 mg/ml; Merk) and
481 cOmplete Protease Inhibitor (Roche). The samples were sonicated and centrifuged at
482 15,000*g* for 45 min at 4°C to pellet cell debris. The cleared lysates were passed through a
483 0.45-µm filter and incubated with 1 ml of Ni-NTA (nitrilotriacetic acid) resin (Thermo
484 Scientific) at 4°C over-night (O/N) on a roller. The beads were washed twice with wash buffer
485 (100mM Tris-HCl (pH 8.0), 300mM NaCl, 10mM Imidazole) and then eluted with a buffer
486 consisting of 100 mM Tris-HCl, 300 mM NaCl, and 500 mM imidazole (pH 8). The eluted
487 proteins were subjected to dialysis in 20mM Tris-HCl, 150mM NaCl and flash-frozen in 20-µl
488 aliquots.

489 For the EMSA, 1 µM of a 32-mer single stranded RNA oligonucleotides corresponding to
490 SARS-CoV-2 (GenBank accession no. MZ558051.1) sequence 5'-
491 CGAGGCCACGCGGAGUACGAUCGAGGGUACAG-3' and a scrambled version thereof, 5'-
492 GGCACGGAGUAUACCGGACGAGCGGAACGGCU-3', each were mixed 1 :1 with their
493 respective complimentary RNA oligonucleotides in denaturing buffer (10 mM $NaH_2PO_4 \cdot H_2O$,
494 50 mM NaCl, 1 mM EDTA, 0.01% NaN_3, pH 7.4 at 25°C), incubated at 90°C for 4 min and then
495 allowed to anneal at RT for 30 min. For the ssRNA sample preparation, the oligonucleotide
496 was diluted in denaturing buffer, incubated at 90°C for 30 sec to destroy possible secondary
497 structures and rapidly cooled on ice. Proteins were diluted in protein buffer (20mM Tris-HCl
498 (pH=8), 150mM NaCl) to a concentration of 100 ng/µl and mixed in 10X, 20X or 40X fold
499 molar excess with 10 ng ssRNA or 10 ng dsRNA in binding buffer (20 mM Tris-HCl, 100 mM
500 NaCl, 1 mM EDTA, 1mM TCEP, 0.02% Tween-20, pH 7.0 at 25°C) in 5 µl reaction volumes. The
501 samples were incubated for 30 min on ice, then supplemented with glycerol to a final
502 concentration of 5% (v/v) and separated in ultrathin (10 ml; 75 x 50 mm) RNase-free 1%
503 agarose gels in 0.5x TB buffer (45 mM Tris base, 45 mM boric acid, pH 8.2-8.5) at 200V. RNAs
504 were stained by incubating the gels in 50 ml 2X Invitrogen™ SYBR™ Gold nucleic acid gel
505 stain (ThermoFisher) in 0.5x TB buffer, diluted from a 10.000X concentrate, for 15 min under
506 agitation and de-stained for 21 min with 0.5 X TB buffer refreshing the buffer 3 times.
507 Stained RNA was visualized with the Gel Doc System (BioRad).
508
509 **Western-blot analysis.** HeLa R19 cells were seeded in 6-well clusters ($4x10^5$ cells/well) and
510 after a 16 hr recovery were infected with recombinant EMCVs at MOI 10. The infection was
511 allowed to proceed for 6 or 8 hours after which cells were released by trypsin and lysed in
512 ice-cold lysis buffer (Tris-HCl pH 8.0, 50mM, NaCl 150mM, EDTA 1mM, NP40 1%, cOmplete
513 Mini Protease Inhibitor Cocktail (Roche) and phosphatase inhibitor PhosSTOP (Roche)) for 30
514 min at 4°C under constant agitation. Cell debris was pelleted for 20 min 12000 rpm at 4°C.
515 Cleared lysates were harvested and protein concentrations determined by the Pierce BCA
516 assay (ThermoFisher Scientific) according to the manufacturer's instructions. Samples of
517 each lysate, corresponding to 100 µg protein, were separated by SDS-PAGE in reducing 10%
518 polyacrylamide gels. The proteins were then blotted onto 0.2 µm nitrocellulose membranes
519 by wet electrophoretic transfer. Membranes were washed three times in TBST (20 mM Tris,
520 150 mM NaCl + 0.1% Tween-20), 5 min each, and incubated in blocking buffer (TBST + 2%

521 BSA) for 1h at RT. Membranes were successively incubated with primary antibodies diluted
522 in blocking buffer (mouse anti-PKR, 1:1000, BD Biosciences; rabbit anti-PKR-P, 1:1000,
523 Abcam; mouse anti-βactin, 1:5000, Invitrogen; rabbit anti-mengovirus capsid, 1:1000, kindly
524 provided by Prof. Ann Palmenberg) for 16 hr at 4°C, and then for 30 min at RT with goat-α-
525 mouse-IRDye680 (Li-COR, 1:15000) or goat-α-rabbit-IRDye800 (Li-COR, 1:15000) diluted in
526 blocking buffer. Between and after the incubations, the membranes were washed, thrice
527 each time, with TBST. Finally, membranes were washed once with PBS and scanned using an
528 Odyssey Imager (Li-COR).
529
530 **RT-qPCR analysis.** HeLa R19 cells, seeded in 24-well clusters (5x10^{4} cells/well), were
531 inoculated with recombinant EMCVs at MOI 10 as above. At 6 or 8 hours post infection cells
532 were lysed and cellular RNA was isolated using the total RNA isolation kit (Machery-Nagel)
533 according to manufacturer's instructions. Reverse transcription was set up using TaqMan
534 Reverse Transcription Reagents (Applied Biosystem) as indicated in the manufacturer's
535 instructions. qPCR analysis of human IFN-β, human actin mRNA and EMCV viral RNA was
536 performed mixing the Fast SYBR green Master Mix (ThermoFisher) with cDNA and 1μM of
537 the forward and reverse corresponding primers: IFN-β (5'-ATGACCAACAAGTGTCTCCTCC-3'
538 and 5'-GCTCATGGAAAGAGCTGTAGTG-3'), actin (5'-CCTTCCTGGGCATGGAGTCCTG-3' and
539 5'GGAGCAATGATCTTGATCTTC-3') and EMCV rna (5'-TCTGTTCTGCCTGTGTTTG-3' and 5'-
540 AAAGAAGAGGGTGCCGAAAT-3'). Amplification occurred in a Roche Light Cycler using the
541 following program: polymerase activation (95°C for 5min), amplification (45 cycles: 95°C for
542 10 sec, 60°C for 5 sec, 72°C for 30 sec), melting curve (95°C for 5 sec, 65°C for 1 min) and
543 cooling (40°C for 10 sec). The experiments were carried out in triplex for each data point.
544 The relative quantification of the IFN-β gene expression was determined using the $2^{-\Delta\Delta Ct}$
545 method (74), then the relative IFN-β mRNA levels were normalized to the EMCV-zn IFN-β
546 mRNA level set as 100.
547
548

ACKNOWLEDGMENTS AND FUNDING SOURCES

We would like to thank Huib H. Rabouw for his constructive feedbacks received for this project.

This work was supported by the European Union (Horizon 2020 Marie Skłodowska-Curie ETN "INITIATE", grant agreement number 813343) and by the Dutch Research Council NWO OCENW.KLEIN.344.

556 **REFERENCES**

557

558 1. S. Hur, Double-Stranded RNA Sensors and Modulators in Innate Immunity. *Annu Rev*
559 *Immunol* **37**, 349-375 (2019).
560 2. D. H. Wreschner, J. W. McCauley, J. J. Skehel, I. M. Kerr, Interferon action--sequence
561 specificity of the ppp(A2'p)nA-dependent ribonuclease. *Nature* **289**, 414-417 (1981).
562 3. J. B. Andersen, K. Mazan-Mamczarz, M. Zhan, M. Gorospe, B. A. Hassel, Ribosomal protein
563 mRNAs are primary targets of regulation in RNase-L-induced senescence. *RNA Biol* **6**, 305-315
564 (2009).
565 4. Y. Li *et al.*, Activation of RNase L is dependent on OAS3 expression during infection with
566 diverse human viruses. *Proc Natl Acad Sci U S A* **113**, 2241-2246 (2016).
567 5. J. Donovan, S. Rath, D. Kolet-Mandrikov, A. Korennykh, Rapid RNase L-driven arrest of
568 protein synthesis in the dsRNA response without degradation of translation machinery. *Rna*
569 **23**, 1660-1671 (2017).
570 6. J. M. Burke, S. L. Moon, T. Matheny, R. Parker, RNase L Reprograms Translation by
571 Widespread mRNA Turnover Escaped by Antiviral mRNAs. *Mol Cell* **75**, 1203-1217.e1205
572 (2019).
573 7. S. L. Schwartz, G. L. Conn, RNA regulation of the antiviral protein 2'-5'-oligoadenylate
574 synthetase. *Wiley Interdiscip Rev RNA* **10**, e1534 (2019).
575 8. A. G. Hinnebusch, The scanning mechanism of eukaryotic translation initiation. *Annu Rev*
576 *Biochem* **83**, 779-812 (2014).
577 9. J. L. Llácer *et al.*, Conformational Differences between Open and Closed States of the
578 Eukaryotic Translation Initiation Complex. *Mol Cell* **59**, 399-412 (2015).
579 10. M. Yoneyama, M. Jogi, K. Onomoto, Regulation of antiviral innate immune signaling by
580 stress-induced RNA granules. *The Journal of Biochemistry* **159**, 279-286 (2016).
581 11. Y. Wu, Z. Zhang, Y. Li, Y. Li, The Regulation of Integrated Stress Response Signaling Pathway
582 on Viral Infection and Viral Antagonism. *Frontiers in Microbiology* **12** (2022).
583 12. N. Kedersha *et al.*, Evidence that ternary complex (eIF2-GTP-tRNA(i)(Met))-deficient
584 preinitiation complexes are core constituents of mammalian stress granules. *Mol Biol Cell* **13**,
585 195-210 (2002).
586 13. M. D. Panas, P. Ivanov, P. Anderson, Mechanistic insights into mammalian stress granule
587 dynamics. *J Cell Biol* **215**, 313-323 (2016).
588 14. S. Hofmann, N. Kedersha, P. Anderson, P. Ivanov, Molecular mechanisms of stress granule
589 assembly and disassembly. *Biochimica et Biophysica Acta (BBA) - Molecular Cell Research*
590 **1868**, 118876 (2021).
591 15. H. l. n. Tourrière *et al.*, The RasGAP-associated endoribonuclease G3BP assembles stress
592 granules. *Journal of Cell Biology* **160**, 823-831 (2003).
593 16. N. Gilks *et al.*, Stress Granule Assembly Is Mediated by Prion-like Aggregation of TIA-1.
594 *Molecular Biology of the Cell* **15**, 5383-5398 (2004).
595 17. J. R. Wheeler, T. Matheny, S. Jain, R. Abrisch, R. Parker, Distinct stages in stress granule
596 assembly and disassembly. *Elife* **5** (2016).
597 18. J. Guillén-Boixet *et al.*, RNA-Induced Conformational Switching and Clustering of G3BP Drive
598 Stress Granule Assembly by Condensation. *Cell* **181**, 346-361.e317 (2020).
599 19. P. Yang *et al.*, G3BP1 Is a Tunable Switch that Triggers Phase Separation to Assemble Stress
600 Granules. *Cell* **181**, 325-345.e328 (2020).
601 20. K. Onomoto *et al.*, Critical role of an antiviral stress granule containing RIG-I and PKR in viral
602 detection and innate immunity. *PLoS One* **7**, e43031 (2012).
603 21. J.-S. Yoo *et al.*, DHX36 Enhances RIG-I Signaling by Facilitating PKR-Mediated Antiviral Stress
604 Granule Formation. *PLOS Pathogens* **10**, e1004012 (2014).

605 22. L. C. Reineke, R. E. Lloyd, The stress granule protein G3BP1 recruits protein kinase R to
606 promote multiple innate immune antiviral responses. *J Virol* **89**, 2575-2589 (2015).
607 23. W. Yang *et al.*, G3BP1 inhibits RNA virus replication by positively regulating RIG-I-mediated
608 cellular antiviral response. *Cell Death & Disease* **10**, 946 (2019).
609 24. X. Deng *et al.*, Coronavirus nonstructural protein 15 mediates evasion of dsRNA sensors and
610 limits apoptosis in macrophages. *Proceedings of the National Academy of Sciences* **114**,
611 E4251-E4260 (2017).
612 25. E. Kindler *et al.*, Early endonuclease-mediated evasion of RNA sensing ensures efficient
613 coronavirus replication. *PLoS Pathog* **13**, e1006195 (2017).
614 26. J. Zhao *et al.*, Coronavirus Endoribonuclease Ensures Efficient Viral Replication and Prevents
615 Protein Kinase R Activation. *J Virol* **95** (2020).
616 27. H. H. Rabouw *et al.*, Middle East Respiratory Coronavirus Accessory Protein 4a Inhibits PKR-
617 Mediated Antiviral Stress Responses. *PLoS Pathog* **12**, e1005982 (2016).
618 28. K. Nakagawa, K. Narayanan, M. Wada, S. Makino, Inhibition of Stress Granule Formation by
619 Middle East Respiratory Syndrome Coronavirus 4a Accessory Protein Facilitates Viral
620 Translation, Leading to Efficient Virus Replication. *J Virol* **92** (2018).
621 29. J. M. Thornbrough *et al.*, Middle East Respiratory Syndrome Coronavirus NS4b Protein
622 Inhibits Host RNase L Activation. *mBio* **7**, e00258 (2016).
623 30. S. A. Goldstein *et al.*, Lineage A Betacoronavirus NS2 Proteins and the Homologous Torovirus
624 Berne pp1a Carboxy-Terminal Domain Are Phosphodiesterases That Antagonize Activation of
625 RNase L. *Journal of Virology* **91**, e02201-02216 (2017).
626 31. H. H. Rabouw *et al.*, Inhibition of the integrated stress response by viral proteins that block p-
627 eIF2–eIF2B association. *Nature Microbiology* **5**, 1361-1373 (2020).
628 32. B. Gao *et al.*, Inhibition of anti-viral stress granule formation by coronavirus
629 endoribonuclease nsp15 ensures efficient virus replication. *PLOS Pathogens* **17**, e1008690
630 (2021).
631 33. T. Cai, Z. Yu, Z. Wang, C. Liang, S. Richard, Arginine methylation of SARS-Cov-2 nucleocapsid
632 protein regulates RNA binding, its ability to suppress stress granule formation, and viral
633 replication. *J Biol Chem* **297**, 100821 (2021).
634 34. L. Luo *et al.*, SARS-CoV-2 nucleocapsid protein phase separates with G3BPs to disassemble
635 stress granules and facilitate viral production. *Sci Bull (Beijing)* **66**, 1194-1204 (2021).
636 35. Z.-Q. Zheng, S.-Y. Wang, Z.-S. Xu, Y.-Z. Fu, Y.-Y. Wang, SARS-CoV-2 nucleocapsid protein
637 impairs stress granule formation to promote viral replication. *Cell Discovery* **7**, 38 (2021).
638 36. D. E. Gordon *et al.*, A SARS-CoV-2 protein interaction map reveals targets for drug
639 repurposing. *Nature* **583**, 459-468 (2020).
640 37. T. Kruse *et al.*, Large scale discovery of coronavirus-host factor protein interaction motifs
641 reveals SARS-CoV-2 specific mechanisms and vulnerabilities. *Nature Communications* **12**,
642 6761 (2021).
643 38. J. Li *et al.*, Virus-Host Interactome and Proteomic Survey Reveal Potential Virulence Factors
644 Influencing SARS-CoV-2 Pathogenesis. *Med (N Y)* **2**, 99-112.e117 (2021).
645 39. M. Biswal, J. Lu, J. Song, SARS-CoV-2 Nucleocapsid Protein Targets a Conserved Surface
646 Groove of the NTF2-like Domain of G3BP1. *Journal of Molecular Biology* **434**, 167516 (2022).
647 40. K. R. Hurst, C. A. Koetzner, P. S. Masters, Identification of In Vivo-Interacting Domains of the
648 Murine Coronavirus Nucleocapsid Protein. *Journal of Virology* **83**, 7221-7234 (2009).
649 41. K. R. Hurst, R. Ye, S. J. Goebel, P. Jayaraman, P. S. Masters, An interaction between the
650 nucleocapsid protein and a component of the replicase-transcriptase complex is crucial for
651 the infectivity of coronavirus genomic RNA. *J Virol* **84**, 10276-10288 (2010).
652 42. C. K. Chang, M. H. Hou, C. F. Chang, C. D. Hsiao, T. H. Huang, The SARS coronavirus
653 nucleocapsid protein--forms and functions. *Antiviral Res* **103**, 39-50 (2014).
654 43. Q. Ye, A. M. V. West, S. Silletti, K. D. Corbett, Architecture and self-assembly of the SARS-CoV-
655 2 nucleocapsid protein. *Protein Sci* **29**, 1890-1901 (2020).

656 44. T. Y. Peng, K. R. Lee, W. Y. Tarn, Phosphorylation of the arginine/serine dipeptide-rich motif
657 of the severe acute respiratory syndrome coronavirus nucleocapsid protein modulates its
658 multimerization, translation inhibitory activity and cellular localization. *Febs j* **275**, 4152-4163
659 (2008).
660 45. E. Nikolakaki, T. Giannakouros, SR/RS Motifs as Critical Determinants of Coronavirus Life
661 Cycle. *Frontiers in Molecular Biosciences* **7** (2020).
662 46. C. A. Koetzner, K. R. Hurst-Hess, L. Kuo, P. S. Masters, Analysis of a crucial interaction
663 between the coronavirus nucleocapsid protein and the major membrane-bound subunit of
664 the viral replicase-transcriptase complex. *Virology* **567**, 1-14 (2022).
665 47. L. Kuo, C. A. Koetzner, K. R. Hurst, P. S. Masters, S. Perlman, Recognition of the Murine
666 Coronavirus Genomic RNA Packaging Signal Depends on the Second RNA-Binding Domain of
667 the Nucleocapsid Protein. *Journal of Virology* **88**, 4451-4465 (2014).
668 48. R. Molenkamp, W. J. Spaan, Identification of a specific interaction between the coronavirus
669 mouse hepatitis virus A59 nucleocapsid protein and packaging signal. *Virology* **239**, 78-86
670 (1997).
671 49. K. R. Hurst, C. A. Koetzner, P. S. Masters, Characterization of a critical interaction between
672 the coronavirus nucleocapsid protein and nonstructural protein 3 of the viral replicase-
673 transcriptase complex. *Journal of virology* **87**, 9159-9172 (2013).
674 50. W. Huang *et al.*, Molecular determinants for regulation of G3BP1/2 phase separation by the
675 SARS-CoV-2 nucleocapsid protein. *Cell discovery* **7**, 69-69 (2021).
676 51. T. Kruse *et al.*, Large scale discovery of coronavirus-host factor protein interaction motifs
677 reveals SARS-CoV-2 specific mechanisms and vulnerabilities. *Nat Commun* **12**, 6761 (2021).
678 52. C.-Y. Chen *et al.*, Structure of the SARS coronavirus nucleocapsid protein RNA-binding
679 dimerization domain suggests a mechanism for helical packaging of viral RNA. *Journal of*
680 *molecular biology* **368**, 1075-1086 (2007).
681 53. M. Yang *et al.*, Structural Insight Into the SARS-CoV-2 Nucleocapsid Protein C-Terminal
682 Domain Reveals a Novel Recognition Mechanism for Viral Transcriptional Regulatory
683 Sequences. *Frontiers in Chemistry* **8** (2021).
684 54. M. Takeda *et al.*, Solution structure of the c-terminal dimerization domain of SARS
685 coronavirus nucleocapsid protein solved by the SAIL-NMR method. *J Mol Biol* **380**, 608-622
686 (2008).
687 55. R. Zhou, R. Zeng, A. von Brunn, J. Lei, Structural characterization of the C-terminal domain of
688 SARS-CoV-2 nucleocapsid protein. *Molecular Biomedicine* **1**, 2 (2020).
689 56. M. P. Robertson *et al.*, The structure of a rigorously conserved RNA element within the SARS
690 virus genome. *PLoS Biol* **3**, e5 (2005).
691 57. C. R. Carlson *et al.*, Phosphoregulation of Phase Separation by the SARS-CoV-2 N Protein
692 Suggests a Biophysical Basis for its Dual Functions. *Mol Cell* **80**, 1092-1103.e1094 (2020).
693 58. E. Nikolakaki *et al.*, RNA association or phosphorylation of the RS domain prevents
694 aggregation of RS domain-containing proteins. *Biochimica et Biophysica Acta (BBA) - General*
695 *Subjects* **1780**, 214-225 (2008).
696 59. S. Wang *et al.*, Targeting liquid–liquid phase separation of SARS-CoV-2 nucleocapsid protein
697 promotes innate antiviral immunity by elevating MAVS activity. *Nature Cell Biology* **23**, 718-
698 732 (2021).
699 60. Y. Zheng *et al.*, SARS-CoV-2 NSP5 and N protein counteract the RIG-I signaling pathway by
700 suppressing the formation of stress granules. *Signal Transduction and Targeted Therapy* **7**, 22
701 (2022).
702 61. S. Nabeel-Shah *et al.*, SARS-CoV-2 nucleocapsid protein binds host mRNAs and attenuates
703 stress granules to impair host stress response. *iScience* **25**, 103562 (2022).
704 62. H. Liu *et al.*, SARS-CoV-2 N Protein Antagonizes Stress Granule Assembly and IFN Production
705 by Interacting with G3BPs to Facilitate Viral Replication. *Journal of Virology* **0**, e00412-00422.

706 63. K. M. Scherer *et al.*, SARS-CoV-2 nucleocapsid protein adheres to replication organelles
707 before viral assembly at the Golgi/ERGIC and lysosome-mediated egress. *Science Advances* **8**,
708 eabl4895 (2022).
709 64. D. C. Dinesh *et al.*, Structural basis of RNA recognition by the SARS-CoV-2 nucleocapsid
710 phosphoprotein. *PLoS pathogens* **16**, e1009100-e1009100 (2020).
711 65. C. A. de Haan, H. Vennema, P. J. Rottier, Assembly of the coronavirus envelope: homotypic
712 interactions between the M proteins. *J Virol* **74**, 4967-4978 (2000).
713 66. L. G. Thorne *et al.*, Evolution of enhanced innate immune evasion by SARS-CoV-2. *Nature*
714 **602**, 487-495 (2022).
715 67. S. Leary *et al.*, Generation of a Novel SARS-CoV-2 Sub-genomic RNA Due to the R203K/G204R
716 Variant in Nucleocapsid: Homologous Recombination has Potential to Change SARS-CoV-2 at
717 Both Protein and RNA Level. *Pathog Immun* **6**, 27-49 (2021).
718 68. S. Lu *et al.*, The SARS-CoV-2 nucleocapsid phosphoprotein forms mutually exclusive
719 condensates with RNA and the membrane-associated M protein. *Nature Communications* **12**,
720 502 (2021).
721 69. D. E. Gordon *et al.*, A SARS-CoV-2 protein interaction map reveals targets for drug
722 repurposing. *Nature* **583**, 459-468 (2020).
723 70. H. Liu *et al.*, SARS-CoV-2 N Protein Antagonizes Stress Granule Assembly and IFN Production
724 by Interacting with G3BPs to Facilitate Viral Replication. *Journal of Virology* **0**, e00412-00422
725 (2022).
726 71. X. Lei *et al.*, Activation and evasion of type I interferon responses by SARS-CoV-2. *Nature*
727 *Communications* **11**, 3810 (2020).
728 72. L. Miorin *et al.*, SARS-CoV-2 Orf6 hijacks Nup98 to block STAT nuclear import and antagonize
729 interferon signaling. *Proceedings of the National Academy of Sciences* **117**, 28344-28354
730 (2020).
731 73. G. M. Duke, A. C. Palmenberg, Cloning and synthesis of infectious cardiovirus RNAs
732 containing short, discrete poly(C) tracts. *J Virol* **63**, 1822-1826 (1989).
733 74. K. J. Livak, T. D. Schmittgen, Analysis of Relative Gene Expression Data Using Real-Time
734 Quantitative PCR and the 2−ΔΔCT Method. *Methods* **25**, 402-408 (2001).
735 75. R. Zhou, R. Zeng, A. von Brunn, J. Lei, Structural characterization of the C-terminal domain of
736 SARS-CoV-2 nucleocapsid protein. *Molecular biomedicine* **1**, 2-2 (2020).

737

738

739 **LEGENDS**

740

741 **Fig. 1. SARS-CoV-2 N inhibits PKR-induced ISR, preventing translation arrest and SG**
742 **formation in HeLa and A549 cells.** (***A***) HeLa and A549 cells were transfected with expression
743 vector pEGFP-N3 (EGFP) or pEGFP-N3 derivatives encoding SARS-CoV-2 N, MERS-4a, IAV-NS1
744 or Bw-CoV-AcP10 genetically fused to EGFP. Induction of the ISR via dsRNA-mediated PKR
745 activation or suppression thereof was assessed by comparing EGFP fluorescence intensity
746 and SG formation as detected by immunofluorescence staining for G3BP2. (left panel)
747 Transfected HeLa cells; (immune)fluorescence microscopy images, representative results.
748 Scale bars: 50 µm. (right panel) Bar graphs for Hela and A549 cells showing the percentage
749 of EGFP expressing cells containing G3BP2-positive SGs. The results are representative of
750 three independent experiments counting >200 cells per sample. Standard deviation
751 indicated by error bars; *** p=0.001, **** p< 0.001, ns = not significant (one-way ANOVA
752 with Dunnett post hoc test). (***B***) HeLa cells were transfected as in A. and treated with 500 µM
753 of sodium arsenite ($NaAsO_2$) to also trigger the ISR by inducing oxidative stress.
754 (Immuno)fluorescence analysis (left panel), quantitative representation of the results and
755 statistical analysis as in A (right panel). (***C***) Inhibition of SG formation and translational arrest
756 by pEGFP-N3-expressed N proteins of MERS-CoV and HCoV-229E. (Immuno)fluorescence
757 analysis (left panel), quantitative representation of the results and statistical analysis as in A.

758

759

760 **Fig. 2. Nucleocapsid domain N2b suppresses translational arrest and SG formation.** (***A***)
761 Schematic representation of truncated derivatives of SARS-CoV-2 N protein fused to EGFP
762 (left panel). The proteins were overexpressed from pEGFP-N3-based vectors in HeLa cells
763 and percentages of SG-positive cells were determined as in Fig. 1A (right panel). The data are
764 representative of three independent experiments with more than 200 cells counted for the
765 presence of G3BP2-positive SGs per individual sample. Standard deviation indicated by error
766 bars. For a statistical analysis of the results, see **Table S1**. (***B***) Representative results from
767 (immuno)fluorescence analysis of HeLa cells transfected to express the SARS-CoV-2 N
768 protein derivatives. Scale bar: 50 µm.

769

770

771 **Fig. 3. N2b mutations that disrupt dsRNA binding abrogate suppression of translational**
772 **arrest and SG formation.** (***A***) (left panel) Cartoon representation of the SARS-CoV-2 N2b
773 dimer (PDB ID code 7C22; (75) generated with PYMOL (pymol.sourceforge.net) with
774 monomers in grey and orange. Top view displaying the positively charged central RNA-
775 binding groove. Side chains of Lys^{257} and Lys^{261}, shown for both monomers and marked
776 for one, in sticks and colored by element with carbon atoms in magenta. (right panel)
777 Electrophoretic mobility shift assay (EMSA) with bacterially expressed N2b and single (ss)
778 and double-stranded (ds) RNA oligonucleotides, designed after SARS-COV-2 stem-loop II
779 motif (s2m). Assays were performed with N2b in 10- or 20-fold molar excess. Non-bound
780 RNA was included as a control (np, no protein). (**B**) The effect of N2b amino acid
781 substitutions on binding of s2m dsRNA (left) or a scrambled version thereof (right). EMSAs
782 performed with N2b and mutant derivatives in 20-fold molar excess. (***C***-***D***) Mutational
783 analysis of SARS-CoV-2 N2b, full-length SARS-CoV-2 N and full-length HCoV-229E N. Select
784 surface-exposed charged residues were substituted by Ala either individually or in
785 combination as indicated and the effect on IRS-induced translational arrest (C) and SG
786 formation (D) was analyzed in HeLa cells as in Fig. 1. For a statistical analysis of the results,
787 see **Table S2**.
788
789
790 **Fig. 4. N-mediated suppression of SG formation and ISR-induced translational arrest is not**
791 **affected by posttranslational modifications or G3BP1/2 interaction.** (***A***) The effect on N-
792 mediated ISR inhibition by mutations introduced to prevent posttranslational modifications
793 ($K^{375}Q$, $K^{375}R$, $R^{95}K$), to disrupt the G3BP1/2 binding site ($R^{14}A+I^{15}A$), to prevent
794 phosphorylation of the SR element (13S>A) or to hamper N2b dimer-dimer interactions (
795 $R^{276}A+R^{293}A$) was tested in HeLa cells by (immune)fluorescence analysis as in Fig. 1. Scale
796 bar: 50 µm. (***B***). Quantification of the results in (A) representative of three independent
797 experiments, with >200 cells counted per sample as in Fig. 1.
798
799
800 **Fig. 5. Quantitative assessment of N-mediated rescue of ISR-induced translational arrest.**
801 HeLa cells were transfected to express EGFP, SARS-CoV-2 N2b, the full-length N proteins of
802 SARS-CoV-2 and HCoV-229E, and mutants thereof from pEGFP-N3-based expression vectors

803 to induce PKR-activated ISR. The capacity of these proteins to rescue translational repression
804 of red fluorescent protein (RFP) *in trans* or lack thereof was measured by flow cytometry at
805 24 hr post transfection (left panels) and fluorescence microscopy (see Fig. S1).
806 Representative flow cytometry histograms shown. The transfected cells were divided into
807 non-RFP-expressing, low (L) RFP-expressing and high (H) RFP-expressing populations (see
808 dashed lines in histograms). For each mutant protein, the [H/L] ratio was calculated and
809 normalized, with those of the corresponding wildtype proteins set at 100%. The bar graphs
810 show mean values with standard deviations based on three independent experiments
811 (unpaired t-test; ****, P<0.001; ns, non-significant) (right).
812
813
814 **Fig. 6. The N2b domain inhibits PKR phosphorylation, prevents SG formation, and reduces**
815 **the type I interferon response in EMCV infected cells.** (***A***) Structure of the polyprotein of
816 recombinant EMCV-L^{zn}-N2aN2b. Schematic representation and a close-up of the N-terminal
817 region with mature cleavage products shown as boxes. Red asterisks indicate the locations
818 of mutations ($C^{19}A/C^{22}A$) in the Zn-finger domain of leader protein L, which abolish its
819 function as EMCV-autologous antagonist of the host innate immune response. The red
820 arrowhead indicates the location of a newly engineered EMCV 3C cleavage site. The yellow
821 box depicts the native N-terminus of the EMCV polyprotein, i.e. the six N-terminal residues
822 of L and two residues encoded by a synthetic *Xho*I cloning site (see Fig. S2 for details). The
823 location of the introduced SARS-CoV-2 N2a2b element is given, with the N2b domain in blue
824 and a Strep2 tag in grey. (***B***) SG formation in EMCV-infected cells is prevented by SARS-CoV-2
825 N2a2b. HeLa cells were infected at MOI 10 with EMCV-L^{zn} recombinant viruses expressing
826 N2a2b or a derivative 'N2a2b-Mut' in which the N2b RNA binding site was abolished by
827 Lys^{257}Ala and Lys^{261}Ala substitutions. Cells infected with parental wildtype EMCV or EMCV-L^{zn}
828 served as controls as were cells infected with recombinant EMCV-L^{zn} derivatives encoding
829 established coronavirus ISR antagonists MERS 4a and BW-Acp10. Cells were fixed at 8 hpi
830 and analyzed by immunofluorescence staining for dsRNA as a marker for infection and for SG
831 scaffold protein G3BP2. (***C***) Percentages of infected cells with stress granules at 6 and 8 hpi.
832 Bar graphs show the means of three independent experiments with more than 200 infected
833 cells counted per sample. Standard deviations indicated by error bars; **** p< 0.0001, ns =
834 not significant (two-way ANOVA with Dunnett post hoc test). (***D***) Western-blot analysis for

835 PKR, phosphorylated PKR (p-PKR), EMCV capsid proteins and β-actin. HeLa cells, mock-
836 infected or infected with recombinant EMCVs at MOI 10, were lysed at 6 or 8 hpi. Images
837 shown are representative of three independent experiments. (***E***) Suppression of type I
838 interferon response in EMCV-infected cells by N2a2b but not N2aN2b-Mut. HeLa cells, mock
839 infected or infected at MOI 10 with the indicated recombinant EMCV-L^{zn} viruses, were lysed
840 at 6 or 8 hpi. Total RNA was isolated and used for RT-qPCR analysis for IFN-β and actin. The
841 IFN-β levels were calculated as fold induction compared to levels in mock-infected cells,
842 after correction for actin mRNA levels, and normalized with EMCV-L^{zn} IFN-β levels set at
843 100%. Data represent means of three independent experiments. Standard deviations
844 indicated by error bars; statistical significance compared to the results for EMCV-L^{zn} or
845 EMCV-L^{zn}-N2aN2b infected cells calculated by two-way ANOVA with the Dunnett post hoc
846 test; ** $p<0.01$; *** $p<0.001$; **** $p<0.0001$.
847
848
849

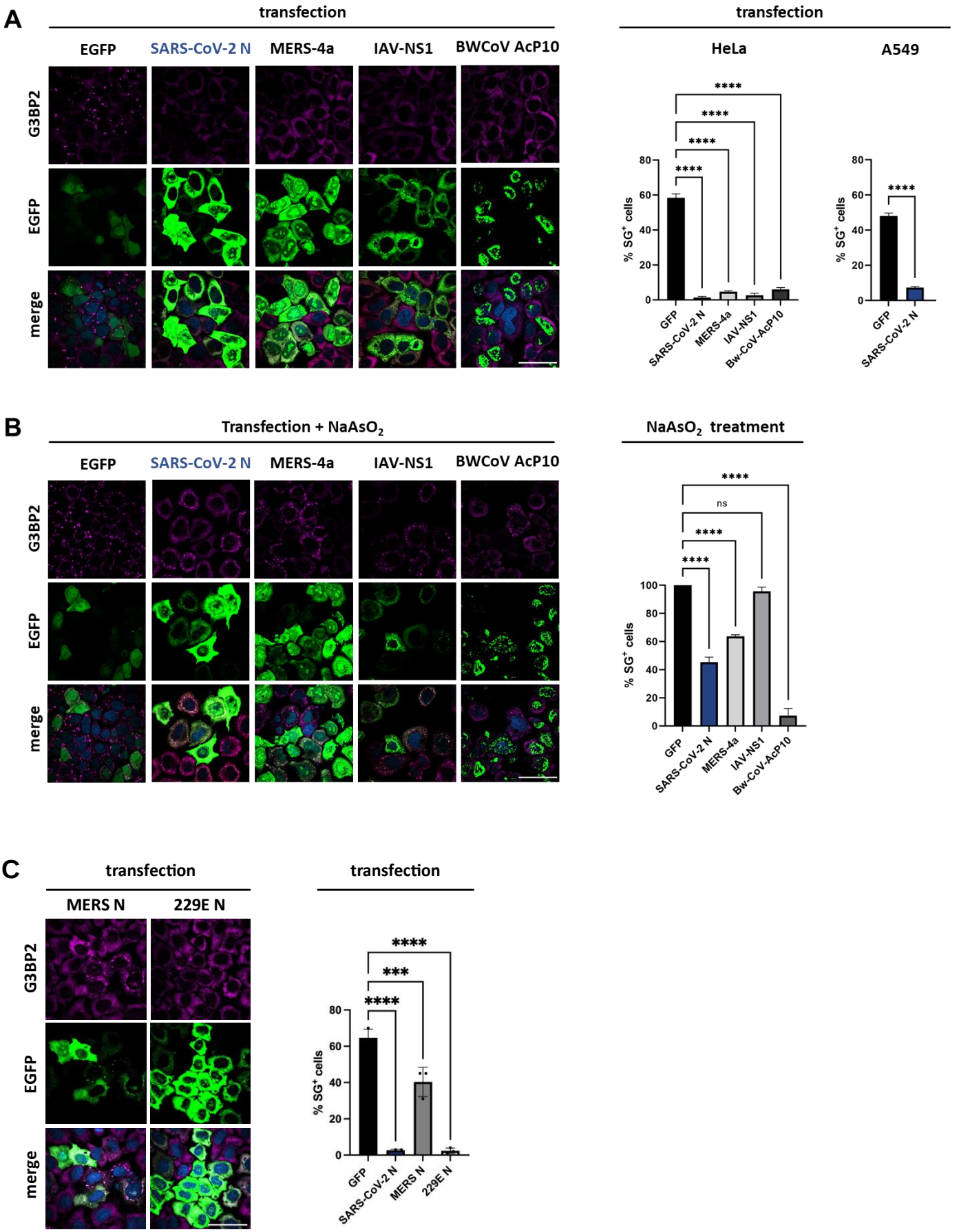
A
transfection
EGFP
SARS-CoV-2 N
MERS-4a
IAV-NS1
BWCoV AcP10
G3BP2
EGFP
merge
transfection
HeLa
A549
% SG+ cells
GFP
SARS-CoV-2 N
MERS-4a
IAV-NS1
Bw-CoV-AcP10
B
Transfection + NaAsO2
NaAsO2 treatment
ns
C
transfection
MERS N
229E N
MERS N
229E N

Fig.1

A

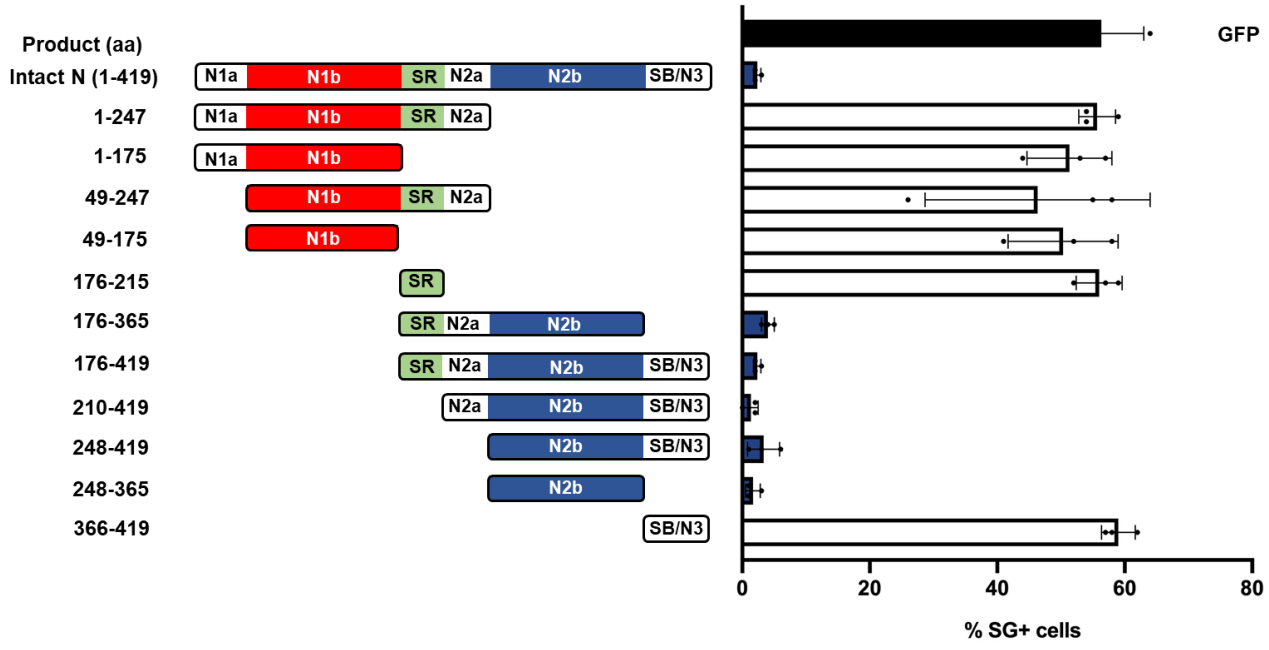
Product (aa)
Intact N (1-419)
1-247
1-175
49-247
49-175
176-215
176-365
176-419
210-419
248-419
248-365
366-419
N1a
N1b
SR
N2a
N2b
SB/N3
GFP
0
20
40
60
80
% SG+ cells

B

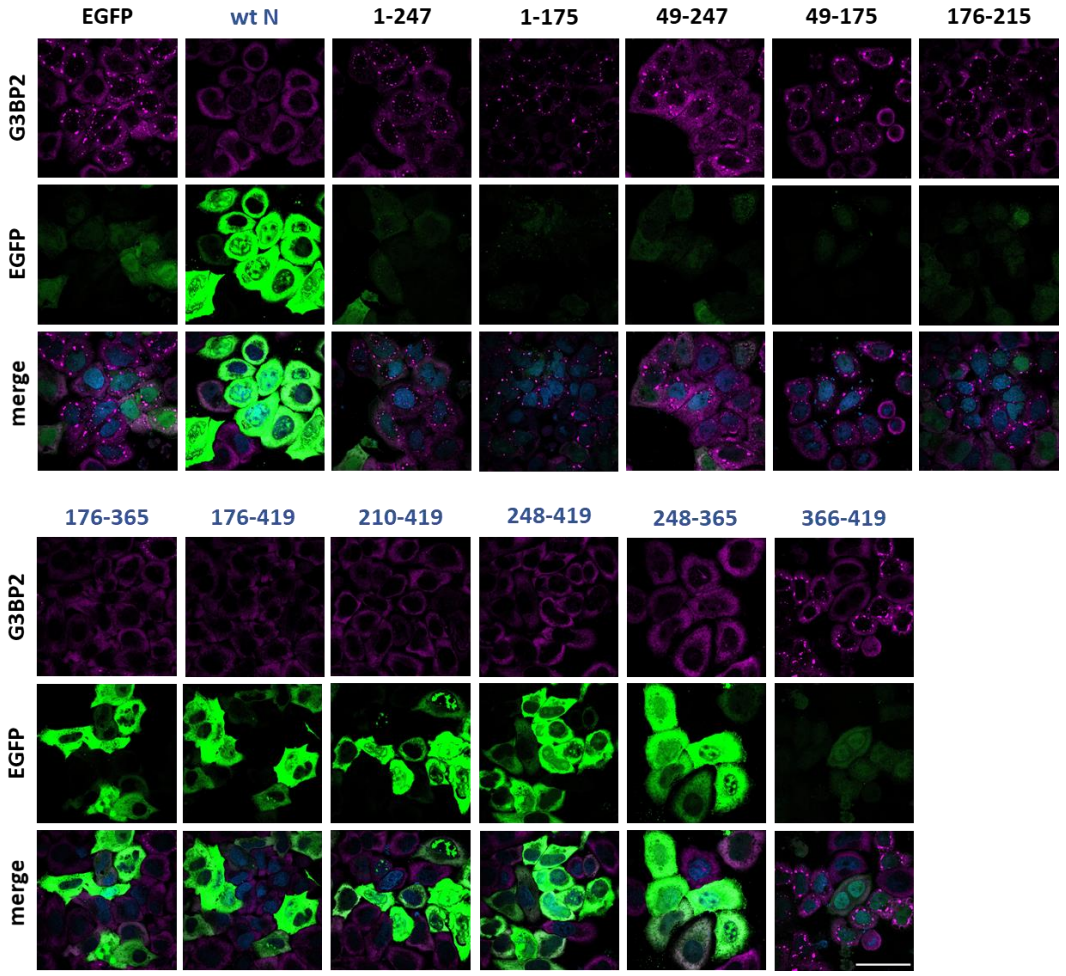
EGFP
wt N
1-247
1-175
49-247
49-175
176-215
176-365
176-419
210-419
248-419
248-365
366-419
G3BP2
EGFP
merge

Fig.2

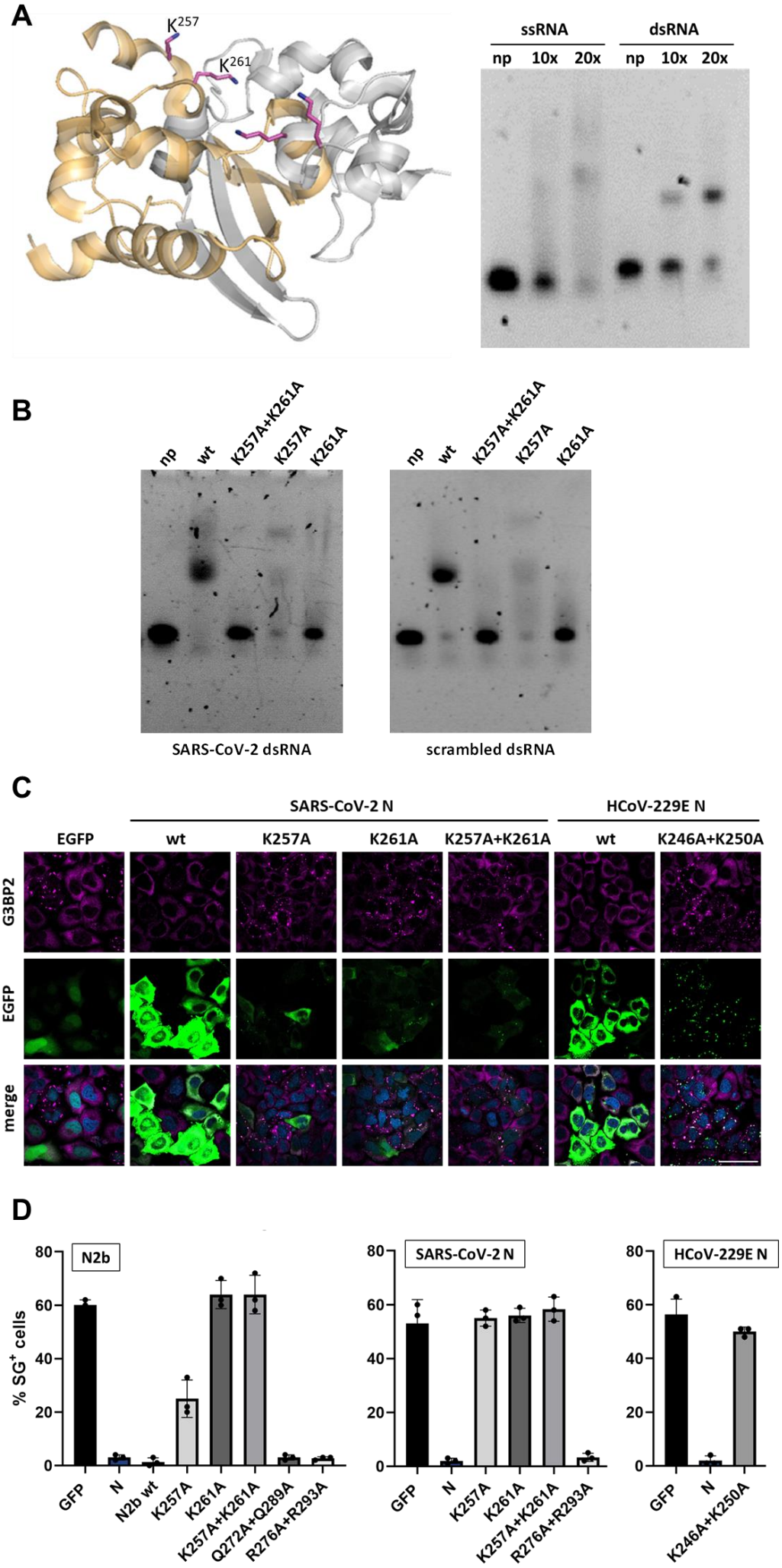
A
K257
K261
ssRNA
dsRNA
np
10x
20x
np
10x
20x
B
np
wt
K257A+K261A
K257A
K261A
np
wt
K257A+K261A
K257A
K261A
SARS-CoV-2 dsRNA
scrambled dsRNA
C
SARS-CoV-2 N
HCoV-229E N
EGFP
wt
K257A
K261A
K257A+K261A
wt
K246A+K250A
G3BP2
EGFP
merge
D
N2b
SARS-CoV-2 N
HCoV-229E N
% SG+ cells
0
20
40
60
80
GFP
N
N2b wt
K257A
K261A
K257A+K261A
Q272A+Q289A
R276A+R293A
K246A+K250A

Fig.3

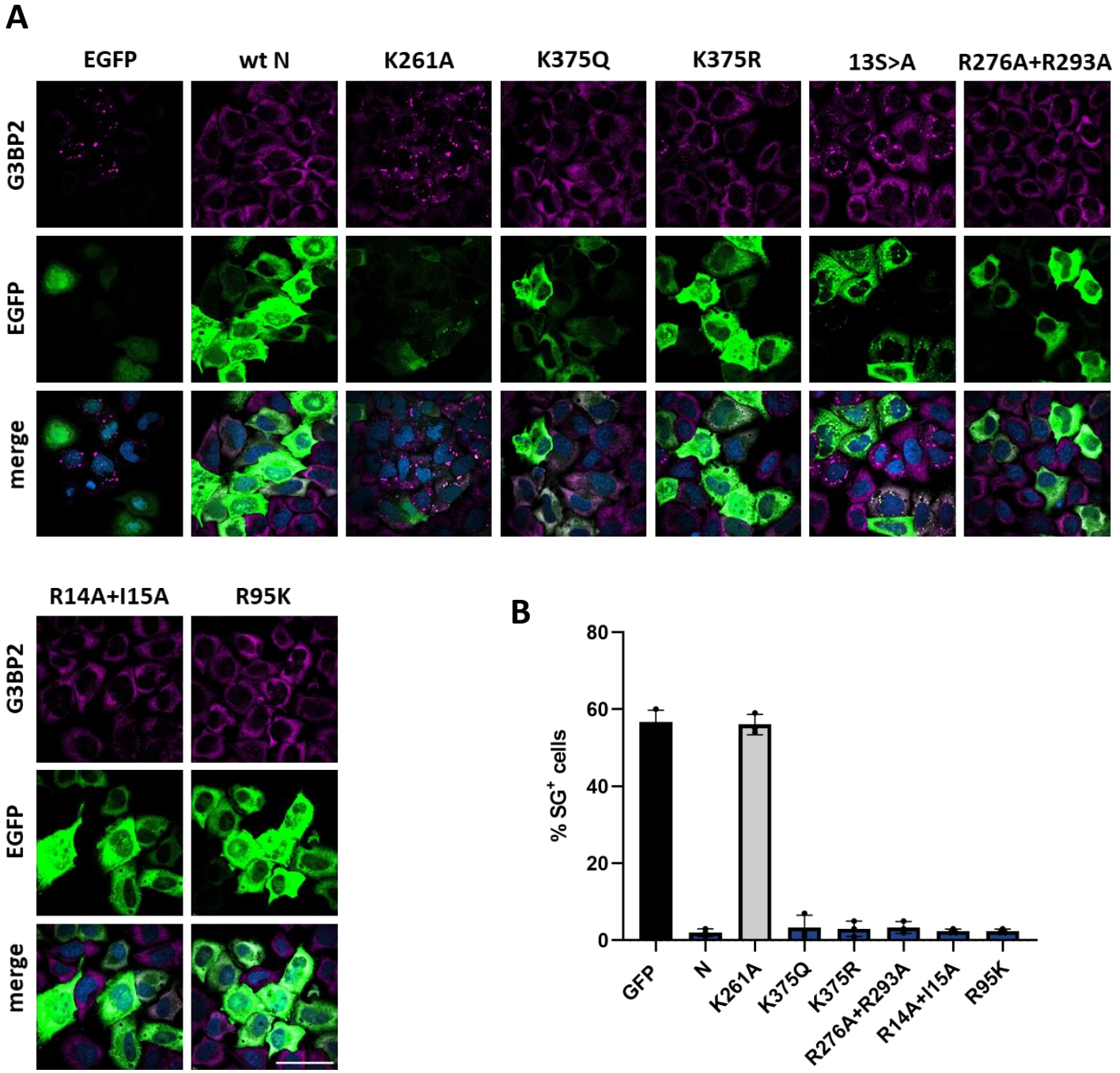
A
EGFP
wt N
K261A
K375Q
K375R
13S>A
R276A+R293A
G3BP2
EGFP
merge
R14A+I15A
R95K
G3BP2
EGFP
merge
B
% SG+ cells
80
60
40
20
0
GFP
N
K261A
K375Q
K375R
R276A+R293A
R14A+I15A
R95K

Fig.4

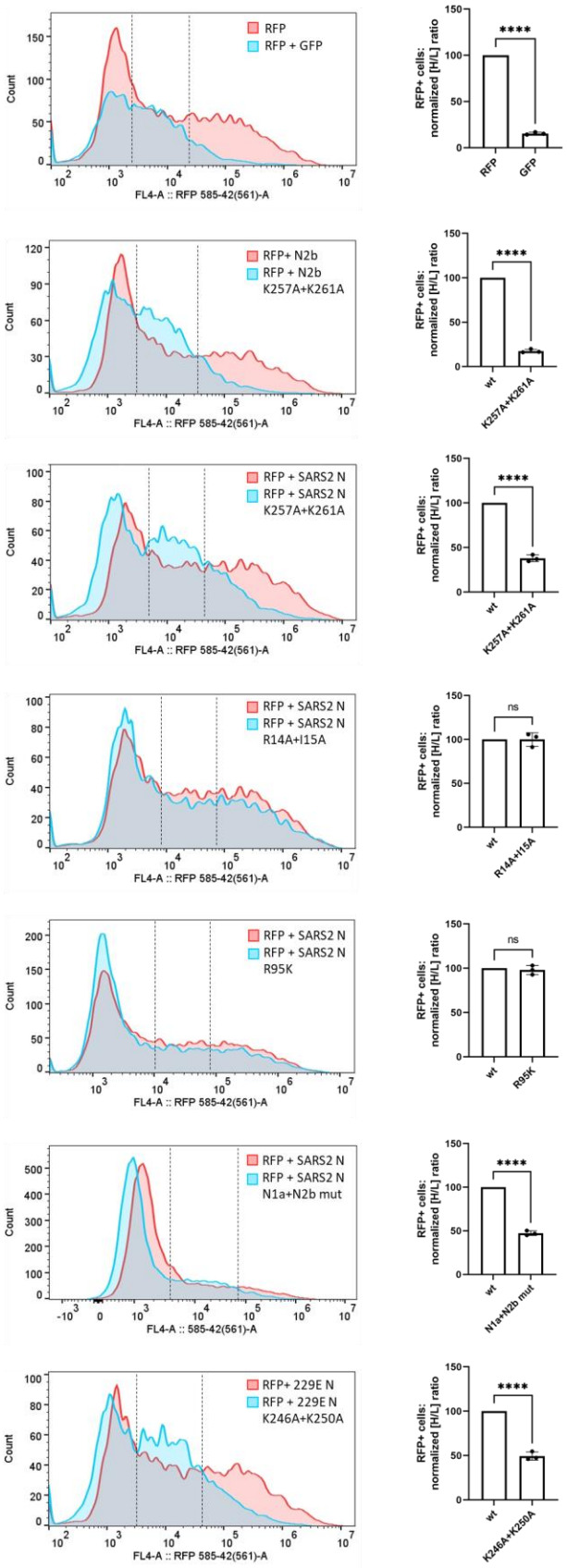
RFP
RFP + GFP
Count
FL4-A :: RFP 585-42(561)-A
RFP+ cells: normalized [H/L] ratio
****
RFP
GFP
RFP+ N2b
RFP + N2b K257A+K261A
wt
K257A+K261A
RFP + SARS2 N
RFP + SARS2 N K257A+K261A
RFP + SARS2 N R14A+I15A
ns
R14A+I15A
RFP + SARS2 N R95K
R95K
RFP + SARS2 N N1a+N2b mut
N1a+N2b mut
RFP+ 229E N
RFP + 229E N K246A+K250A
K246A+K250A

Fig.5

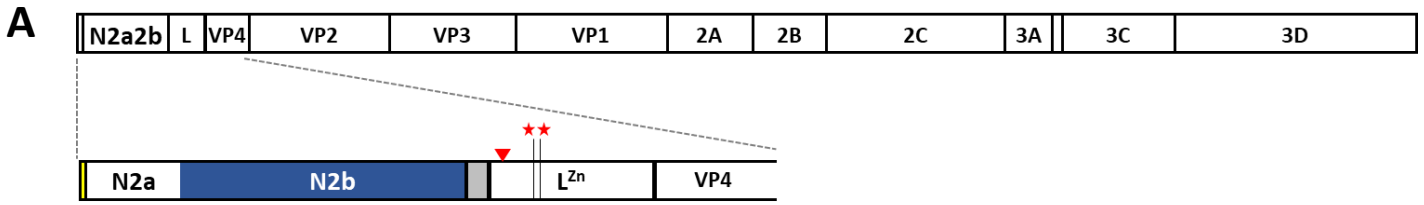
A
N2a2b
L
VP4
VP2
VP3
VP1
2A
2B
2C
3A
3C
3D
N2a
N2b
L^Zn
VP4

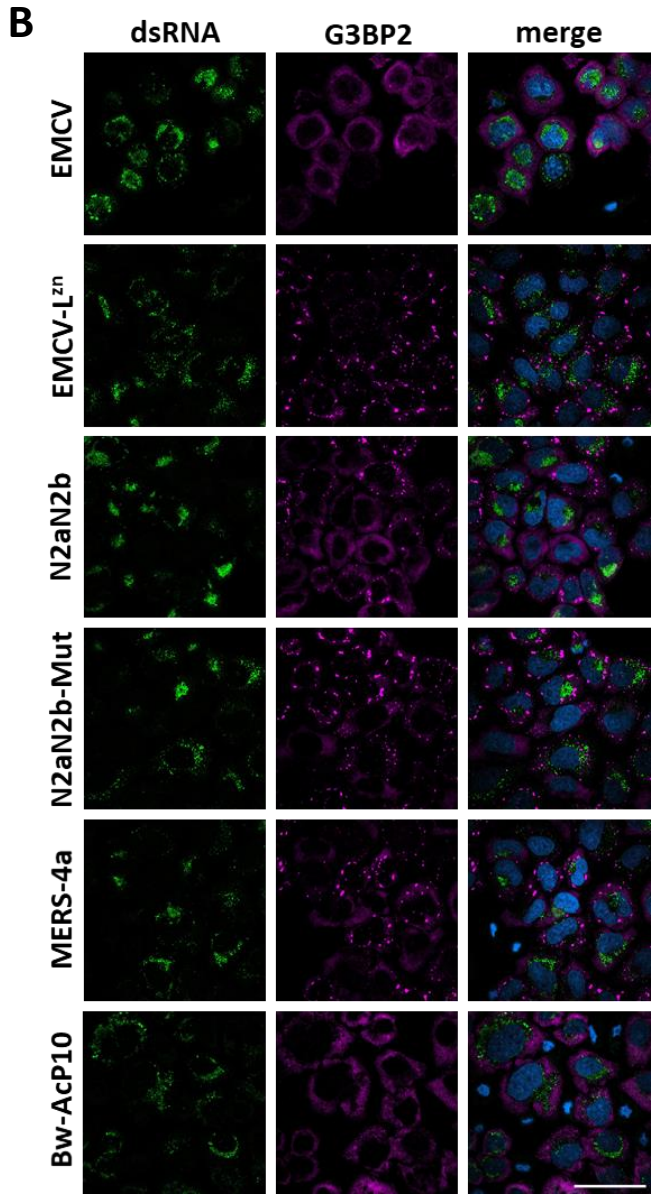
B
dsRNA
G3BP2
merge
EMCV
EMCV-L^zn
N2aN2b
N2aN2b-Mut
MERS-4a
Bw-AcP10

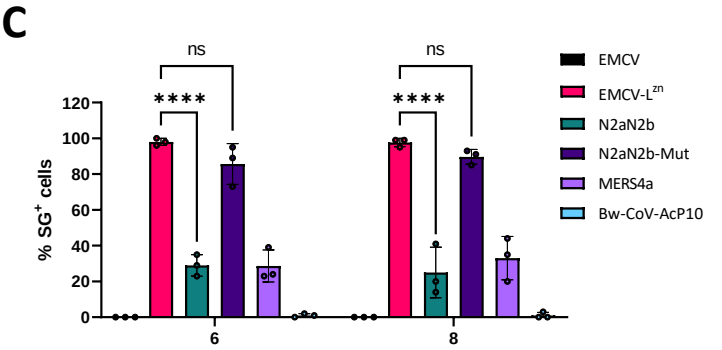
C
ns
****
ns
****
% SG+ cells
120
100
80
60
40
20
0
6
8
EMCV
EMCV-L^zn
N2aN2b
N2aN2b-Mut
MERS4a
Bw-CoV-AcP10

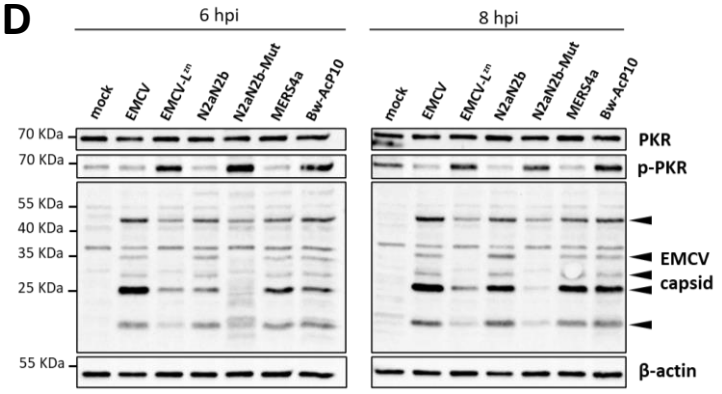
D
6 hpi
8 hpi
mock
EMCV
EMCV-L^zn
N2aN2b
N2aN2b-Mut
MERS4a
Bw-AcP10
70 KDa
70 KDa
55 KDa
40 KDa
35 KDa
25 KDa
55 KDa
PKR
p-PKR
EMCV
capsid
β-actin

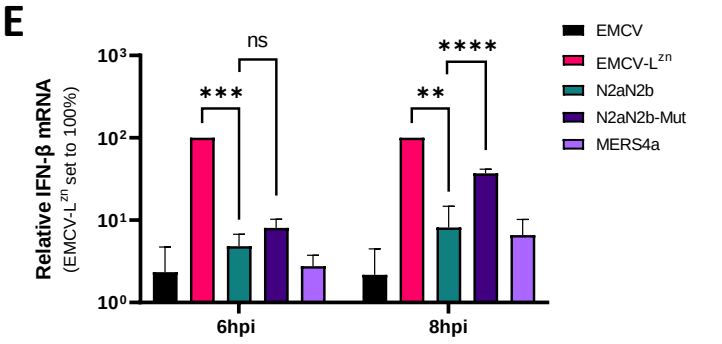
E
Relative IFN-β mRNA
(EMCV-L^zn set to 100%)
10^3
10^2
10^1
10^0
ns
***
****
**
6hpi
8hpi
EMCV
EMCV-L^zn
N2aN2b
N2aN2b-Mut
MERS4a

Fig.6